

Article

Knowledge-Enhanced Deep Learning for Simulation of Extratropical Cyclone Wind Risk

Reda Snaiki ¹  and Teng Wu ^{2,*}

¹ Department of Construction Engineering, École de Technologie Supérieure, University of Quebec, Montreal, QC H3C 1K3, Canada; reda.snaiki@etsmtl.ca

² Department of Civil, Structural and Environmental Engineering, University at Buffalo, Buffalo, NY 14260, USA

* Correspondence: tengwu@buffalo.edu

Abstract: Boundary-layer wind associated with extratropical cyclones (ETCs) is an essential element for posing serious threats to the urban centers of eastern North America. Using a similar methodology for tropical cyclone (TC) wind risk (i.e., hurricane tracking approach), the ETC wind risk can be accordingly simulated. However, accurate and efficient assessment of the wind field inside the ETC is currently not available. To this end, a knowledge-enhanced deep learning (KEDL) is developed in this study to estimate the ETC boundary-layer winds over eastern North America. Both physics-based equations and semi-empirical formulas are integrated as part of the system loss function to regularize the neural network. More specifically, the scale-analysis-based reduced-order Navier–Stokes equations that govern the ETC wind field and the European Centre for Medium-Range Weather Forecasts (ECMWF) Re-Analysis (ERA) ERA-interim data-based two-dimensional (2D) parametric formula (with respect to radial and azimuthal coordinates) that prescribes an asymmetric ETC pressure field are respectively employed as rationalism-based and empiricism-based knowledge to enhance the deep neural network. The developed KEDL, using the standard storm parameters (i.e., spatial coordinates, central pressure difference, translational speed, approach angle, latitude of ETC center, and surface roughness) as the network inputs, can provide the three-dimensional (3D) boundary-layer wind field of an arbitrary ETC with high computational efficiency and accuracy. Finally, the KEDL-based wind model is coupled with a large ETC synthetic track database (SynthETC), where 6-hourly ETC center location and pressure deficit are included to effectively assess the wind risk along the US northeast coast in terms of annual exceedance probability.

Keywords: knowledge-enhanced deep learning; extratropical cyclones; nor'easters; boundary-layer winds; risk analysis



Citation: Snaiki, R.; Wu, T. Knowledge-Enhanced Deep Learning for Simulation of Extratropical Cyclone Wind Risk. *Atmosphere* **2022**, *13*, 757. <https://doi.org/10.3390/atmos13050757>

Academic Editor: Mario Marcello Miglietta

Received: 25 March 2022

Accepted: 4 May 2022

Published: 8 May 2022

Publisher's Note: MDPI stays neutral with regard to jurisdictional claims in published maps and institutional affiliations.



Copyright: © 2022 by the authors. Licensee MDPI, Basel, Switzerland. This article is an open access article distributed under the terms and conditions of the Creative Commons Attribution (CC BY) license (<https://creativecommons.org/licenses/by/4.0/>).

1. Introduction

Considered as large low-pressure systems that affect the North American Atlantic coast, the extratropical cyclones (ETCs), also denoted as nor'easters (over eastern North America), can generate strong winds [1–3], heavy precipitations (rain and/or snow) [4], and storm surge [5]. These hazards are of great significance since they can cause widespread damage to various civil structures and infrastructure systems and are responsible for great economic and life losses [6,7]. Significant efforts have been made to study the tropical cyclones (TCs), while comparatively less research efforts are devoted to ETCs, especially in the engineering field. The ETCs differ in structure and size from the TCs. The latter are characterized by a warm core with energy resulting from the vertical temperature difference between the upper and lower atmosphere, while the former are considered as cold-core cyclones with energy resulting from the horizontal temperature difference between warm and cold air masses. Nor'easters are the dominant cause of extreme wintertime weather in the eastern North America [2], therefore, it is crucial to estimate their related hazard

probabilities and induced risk. The track approach typically used to simulate synthetic storm events is commonly employed for the risk estimation of TC events. However, synthetic ETC track generation is much less used for winter storm hazard and has not been implemented to estimate the ETC hazard probabilities. On the other hand, the effectiveness of this statistical approach is highly related to the employed hazard models. Since the boundary-layer wind of ETCs is an essential element for inflicting widespread damage, accurate and efficient modeling of the wind field is critical to effective mitigation of losses due to ETCs-related hazards.

A number of schemes have been developed to simulate TC boundary-layer winds, such as the empirical or semi-empirical vertical wind profiles [8,9], slab or depth-averaged wind models [10,11], linear height-resolving wind models [12–14], and nonlinear height-resolving wind fields (e.g., Weather Research and Forecasting model). ETC wind, however, is currently obtained by fusing high-fidelity wind models and observational data, due partly to their complicated structure [15,16]. Although these time-consuming schemes are promising to accurately capture ETC wind hazard, they are not suited for probability and risk analysis. Data-driven modeling (e.g., artificial neural networks (ANNs)) techniques have recently gained popularity in wind field simulations [17,18] and other applications [19–22] due to their high efficiency and accuracy. With the rapid development of efficient training algorithms for deep networks, they may shed light on effective prediction of ETC boundary-layer winds. However, the use of black-box deep networks usually requires a large number of high-quality input-output datasets during the training process. This challenge is especially serious for many engineering applications, due partially to the high cost of data generation (using numerical/experimental/field-measurement approach) [23]. To this end, a more data-efficient ANN approach is needed. Dissanayake and Phan-Thien [24] proposed a novel ANN-based solution of the nonlinear partial differential equations (PDEs) by using the governing equations as part of the loss function to regularize the learning process. This scheme has been further advanced to a physics-informed neural network [25,26]. Recently, Snaiki and Wu [27] proposed a more general knowledge-enhanced deep learning (KEDL) to simulate TC wind field by leveraging rationalism-/empiricism-based knowledge through the loss function, where the storm parameters are treated as the network inputs. The developed KEDL significantly enhanced the purely data-driven approach by reducing the required amount of training datasets and presented improved interpolation and extrapolation results than those from the standard neural networks due to its physical constraints.

In this study, a KEDL algorithm is proposed to predict the spatial distribution of Nor'easters boundary-layer winds with high computational efficiency and simulation accuracy. Both physics-based equations and semi-empirical formulas governing the wind field inside ETC boundary layer are integrated as part of the system loss function to regularize the neural network. More specifically, the scale-analysis-based reduced-order Navier–Stokes equations that govern the ETC wind field and the European Centre for Medium-Range Weather Forecasts (ECMWF) Re-Analysis (ERA) ERA-Interim [28] data-based two-dimensional (2D) parametric formula (with respect to radial and azimuthal coordinates) that prescribes an asymmetric ETC pressure field are respectively employed as the rationalism-based and empiricism-based knowledge to enhance the deep neural network. The developed KEDL, using the standard storm parameters (i.e., spatial coordinates, central pressure difference, translational speed, approach angle, latitude of ETC center and surface roughness) as the network inputs, can provide the 3D boundary-layer wind field of an arbitrary ETC with high computational efficiency and accuracy. Finally, the KEDL-based wind model is coupled with a large ETC synthetic track database (SynthETC) [2], where 6-hourly ETC center location and pressure deficit are included to effectively assess the wind risk along the US northeast coast in terms of annual exceedance probability.

2. ETC Background

2.1. Conceptual Model

Nor'easters are large low-pressure systems that affect the North American Atlantic coast and are characterized by distinct fronts that separate the cold and warm air masses. They acquire energy from the horizontal temperature differential, and typically form during the winter season along the U.S. mid-Atlantic coast and move northeastward [29–31]. While the intensity of nor'easters is in general weaker than that of hurricanes, these ETCs can cause significant damage since their occurrence is relatively more frequent and duration is longer, due essentially to the slow movement [31,32].

Two conceptual models were developed to represent the complex structure and general evolution of ETCs using general cyclone characteristics identified from the surface observations, satellite imagery and radar data [28,33]. The first model, denoted as the Norwegian cyclone model [34], describes the ETC evolution from the genesis to the occlusion stage. In this model, a warm air mass and a cold one are separated by a front, where the warm air flows over the cold air with a cyclonic rotation. The other conceptual model, proposed by Shapiro and Keyser [35], describes a more refined life cycle of ETCs based on the remote sensing techniques and space-borne observations, where the cold front fractures away from the warm front and they are completely separated at the cyclone center.

2.2. Composite Analysis

Individual ETCs usually present large case-to-case variability [36–38], hence, the composite analysis is typically employed to underline the most essential features of the ETC structure (e.g., large-scale coherent structure) and evolution characteristics [28]. Furthermore, the case-to-case variability could be significantly reduced, and the identified features are more accurate by restricting the composites to special categories (e.g., intense ETCs) [38–40]. To this end, the reanalysis due to its homogenous and comprehensive results has become an important and popular technique for studying ETCs [41,42]. Specifically, the reanalysis results are generated as a combination of numerical weather prediction systems and atmospheric observations at a typical 6-h frequency based on data assimilation techniques. In this study, the most intense nor'easters from 1989 to 2009, extracted from the ERA-Interim data with a horizontal resolution of 80 km and 60 vertical hybrid levels [43,44], will be utilized to construct the ETC essential structure including the wind and pressure fields, where ETC tracks have been identified using the filtered 850 hPa relative vorticity with a temporal resolution of 6 h [28]. It is shown that the pressure contour is not a circular-type shape, as would be expected from a TC system, but rather presents an elliptic-type shape with an elongated profile in the upper right quadrant [45,46]. Accordingly, it is expected that the pressure field would be better characterized by a function of both the radial and azimuthal coordinates.

2.3. ETC Wind Risk Assessment

To estimate the hazard probabilities and subsequently the ETC wind risk, several approaches have been implemented. The single site probability approach, pioneered by Russel [47], has been implemented to estimate the site-specific statistics of the key storm parameters (e.g., central pressure). This approach involves a Monte Carlo step which samples from the statistical distribution of each storm parameter. Then, a ETC wind model driven by the sampled storm parameters is employed to efficiently generate the corresponding hazard probabilities. However, this approach is only valid for a single site and the limited record data prevents it from accurately estimating the tails of probability density functions. Alternatively, the American Federal Emergency Management Agency (FEMA) has adopted another approach in which a small number of intense historical ETCs are first selected and perturbed. However, this approach fails to exploit the important information provided by those ETCs close to a target region without making landfall [48]. Recently, a most advanced technique, dubbed the track approach, has been widely utilized especially for TC events. This approach generates large databases of full-track synthetic events [2,49]. A key feature

of this methodology is its capability of projecting information from a wider geographic range onto the target region. Therefore, it is capable of determining the annual probability of low-frequency high-impact events. For instance, Hall and Booth [2] successfully generated a statistical model trained on historical ETC tracks to estimate the frequency and intensity of the most severe ETCs. However, no hazard model was coupled with their generated tracks. Considering machine learning techniques are very good at addressing unresolved complexities by extracting hidden informative features from data, they offer a great promise for ETC risk assessment. However, current machine learning and deep learning applications have not been utilized yet for such a purpose. Actually, most of these applications are devoted to the simple detection of ETCs from aerial/satellite imagery and remote sensing data [50–52]. More research efforts are needed to leverage the full potential of machine learning techniques in solving ETC risk-related problems.

3. Methodology

3.1. Knowledge-Enhanced Deep Learning for ETC Boundary-Layer Wind

One challenge in the application of machine learning techniques and specifically deep neural networks (DNNs) to many engineering applications is the requirement of a large number of high-fidelity data which may not be available. Furthermore, these black-box networks are only constrained by the available data, and hence they are usually criticized for poor interpolation/ extrapolation performance especially under noisy environment. By leveraging rationalism-/empiricism-based knowledge through the loss function, the purely data-driven approach might be significantly enhanced, leading to a more general machine learning technique denoted here as knowledge-enhanced deep learning networks (KEDLs), as illustrated in Figure 1.

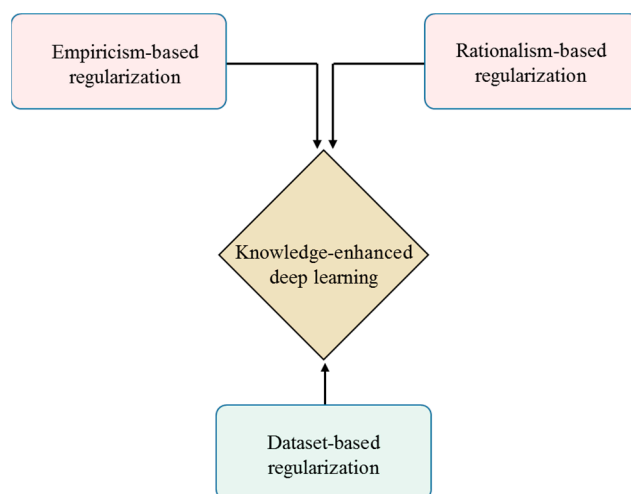


Figure 1. Schematic of knowledge-enhanced deep learning.

3.1.1. Rationalism-Based Knowledge

In the boundary layer of an ETC, the wind fields are governed by the three-dimensional (3D) Navier–Stokes equations [53]:

$$\frac{\partial \vec{v}}{\partial t} + \vec{v} \cdot \nabla \vec{v} = -\frac{1}{\rho} \nabla p - (2\Omega \sin \varphi) \vec{k} \times \vec{v} + \vec{F} \tag{1}$$

where \vec{v} = wind velocity; Ω = rotation rate of the Earth; φ = latitude; \vec{k} = unit vector in the vertical direction; p = pressure; ρ = air density; and \vec{F} = frictional force. A straightforward

scale analysis of Equation (1) leads to the following equations, which are expressed in a cylindrical coordinate system (r, θ, z) as [13]:

$$\frac{\partial u}{\partial t} + u \frac{\partial u}{\partial r} + \frac{v}{r} \frac{\partial u}{\partial \theta} + w \frac{\partial u}{\partial z} - \frac{v^2}{r} - (2\Omega \sin \varphi)v = -\frac{1}{\rho} \frac{\partial p}{\partial r} + K_m \frac{\partial^2 u}{\partial z^2} \quad (2)$$

$$\frac{\partial v}{\partial t} + u \frac{\partial v}{\partial r} + \frac{v}{r} \frac{\partial v}{\partial \theta} + w \frac{\partial v}{\partial z} + \frac{uv}{r} + (2\Omega \sin \varphi)u = -\frac{1}{\rho r} \frac{\partial p}{\partial \theta} + K_m \frac{\partial^2 v}{\partial z^2} \quad (3)$$

where (u, v, w) = wind velocity components with respect to the cylindrical coordinate system (r, θ, z) and K_m = eddy viscosity. In addition, the continuity equation for the case of incompressible flow is expressed as:

$$\frac{1}{r} \frac{\partial ru}{\partial r} + \frac{1}{r} \frac{\partial v}{\partial \theta} + \frac{\partial w}{\partial z} = 0 \quad (4)$$

Two boundary conditions are required for the solution of the ETC wind field components, namely at the upper atmosphere and near the ground surface. The widely used bulk formulation with drag coefficient C_D is utilized at the surface level as [15]:

$$K_m \frac{\partial u}{\partial z} \Big|_{z=0} = C_D u \sqrt{u^2 + v^2} \quad (5)$$

$$K_m \frac{\partial v}{\partial z} \Big|_{z=0} = C_D v \sqrt{u^2 + v^2} \quad (6)$$

At the top of ETC boundary layer, gradient wind balance is established where pressure gradient force balances centrifugal and Coriolis forces [54]. Accordingly, the frictional wind components are negligible, and hence the gradient wind component can be analytically determined as [54,55]:

$$v_g = \frac{-c \sin(\theta - \theta_0) - (2\Omega \sin \varphi)r}{2} + \sqrt{\left(\frac{c \sin(\theta - \theta_0) + (2\Omega \sin \varphi)r}{2}\right)^2 + \frac{r}{\rho} \frac{\partial p}{\partial r}} \quad (7)$$

where c = ETC translational wind speed; and θ_0 = approach angle (counterclockwise positive from the East). It should be noted that the unsteady term related to the gradient wind is expressed as $-c \cdot \nabla v_g$. On the other hand, the unsteady term related to the frictional wind can be ignored since it is significantly smaller than turbulence viscosity and inertia terms. It is noted that the ETC thermodynamics is usually independently examined or weakly coupled with ETC dynamics in engineering applications, and hence not considered in this study.

3.1.2. Parametric Pressure Field

Solving the coupled wind-pressure system is extremely challenging, therefore an alternative approach consists of prescribing the pressure field based on field-measurement data as it is usually done for TC systems. While the pressure field is typically assumed to be symmetric inside TCs, the complex ETC structure imposes an azimuthally dependent pressure profile. To this end, a 2-D parametric formula of the asymmetric pressure field based on the ERA-Interim data is developed in this study. To derive an empirical expression of the pressure field, the composite ETC pressure radial variation at various azimuthal locations will be first examined [28]. As shown in Figure 2, the surface pressure varies with respect to both radial and azimuthal spatial coordinates.

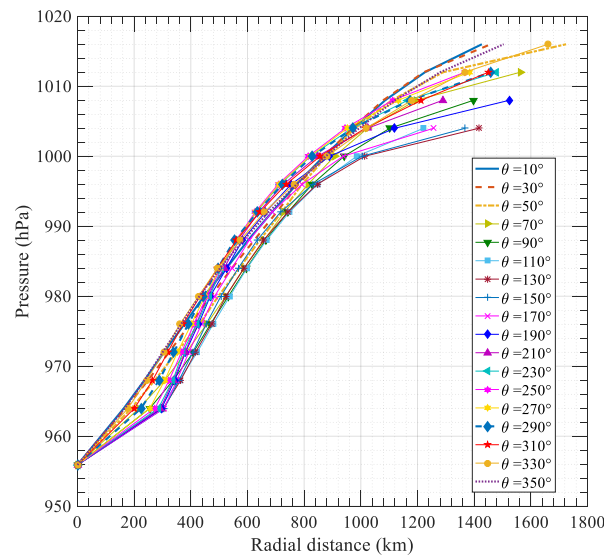


Figure 2. Radial profiles of the composite pressure inside ETC at various azimuthal locations.

Based on the inspection of the collected data, it is found that the pressure field can be fitted by two different profiles corresponding to the cold and warm sectors, respectively. Inspired by the work of Holland [56], a generalized ETC pressure formula is accordingly proposed as:

$$p(r, \theta) = p_c + \Delta p \left\{ \delta \exp \left[- \left(\frac{r_m(\theta)}{r} \right)^{B(\theta)} \right] + (1 - \delta) \left(\frac{r}{r_{size}(\theta)} \right)^{n(\theta)} \right\} \quad (8)$$

where p_c = central pressure; Δp = central-pressure deficit; $r_m(\theta)$ = radius of maximum winds; $B(\theta)$ = shape parameter; $r_{size}(\theta)$ = ETC size (defined as the distance from the ETC center to the outermost closed isobar); and $\delta = 1$ for the cold sector while it is zero for the warm sector. It is quite challenging to accurately identify the limits between the cold and warm sectors (i.e., fronts) at the current stage, therefore, a simplified formula is adopted here and expressed as:

$$p(r, \theta) = p_c + \Delta p \exp \left[- \left(\frac{r_m(\theta)}{r} \right)^{B(\theta)} \right] \quad (9)$$

Similarly in TC cases, the radius of maximum winds $r_m(\theta)$ and the shape factor $B(\theta)$ for ETCs are functions of storm parameters [57]. In this study, they are expressed as:

$$r_m = a_{r_m} + b_{r_m} p_c + c_{r_m} \ln(\varphi) \quad (10)$$

$$B = \alpha_B + \beta_B r_m + \gamma_B \varphi \quad (11)$$

where $a_{r_m}(\theta) = \frac{(1-\varepsilon_1^2)a_1}{1+\varepsilon_1 \cos(\theta-\theta_1)}$; $b_{r_m}(\theta) = -\frac{(1-\varepsilon_2^2)a_2}{1+\varepsilon_2 \cos(\theta-\theta_2)}$; $c_{r_m}(\theta) = \frac{(1-\varepsilon_3^2)a_3}{1+\varepsilon_3 \cos(\theta-\theta_3)}$; and the parameter values for $\varepsilon_1(0.4)$, $\varepsilon_2(0.3606)$, $\varepsilon_3(0.2025)$, $a_1(2941.2)$, $a_2(3.7863)$, $a_3(302.0039)$, $\theta_1(37.6284)$, $\theta_2(48.9242)$, $\theta_3(92.8592)$, $\alpha_B(0.7703)$, $\beta_B(0.0019)$ and $\gamma_B(0.0021)$ are obtained using the Levenberg–Marquardt algorithm [58,59]. It is important to note that the resolution in ERA-interim data could potentially affect the derived pressure, and the use of higher-resolution National Aeronautics and Space Administration (NASA) Modern Era-Retrospective Analysis for Research and Applications (MERRA) reanalysis data may provide better simulation results. In addition, the predefined regression equations (i.e., Equations (8) and (9)) of ETC pressure field may be further improved for modeling such a complex system.

3.1.3. Knowledge-Enhanced Deep Learning Formalization

In this study, ETC boundary-layer winds are approximated by a fully connected, feedforward KEDL system with a hyperbolic tangent activation function and a network architecture of 8-100-100-100-100-100-3. The inputs required for the ETC boundary-layer wind simulation are the spatial coordinates (r, θ, z) and the ETC parameters denoted as $\alpha = [\Delta p; c; \theta_0; \varphi; z_0]$ where z_0 is the surface roughness (to obtain the drag coefficient through $C_D = \frac{\kappa^2}{[\ln(\frac{10}{z_0})]^2}$ and $\kappa =$ von Karman constant). The three model outputs of (u, v, w) representing the wind velocity components with respect to the cylindrical coordinate system (r, θ, z) . While there is a lack of general rules for the determination of the optimal model architecture [60], an exhaustive trial-and-error approach is usually followed [61]. A simplified representation of the KEDL architecture is presented in Figure 3, where the governing equations-based cost functions (Cf_1, Cf_2, Cf_3) and the boundary condition-based cost functions (Cf_4, Cf_5, Cf_6) are incorporated in the system.

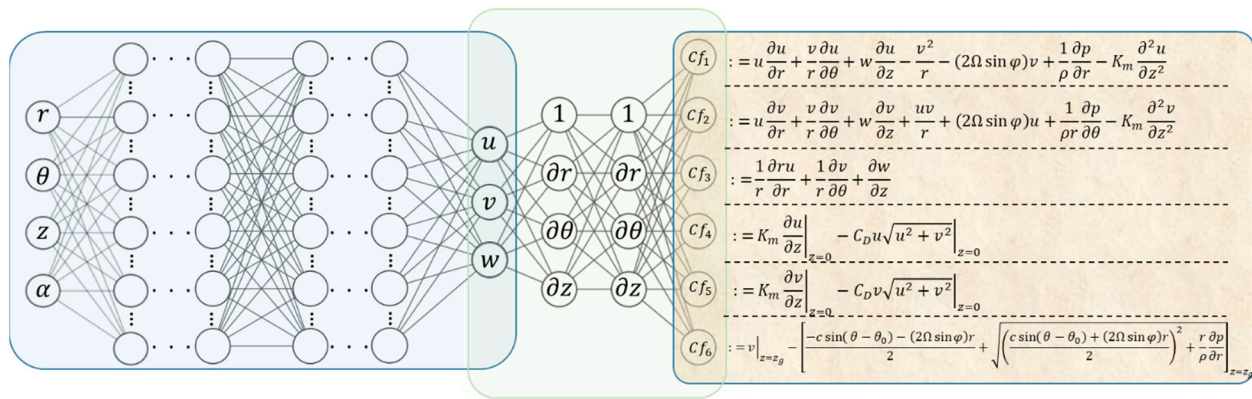


Figure 3. Knowledge-enhanced deep network architecture for ETC.

The total cost function can be then expressed as:

$$\mathcal{L} = \frac{\gamma_d}{N_d} \sum_{j=1}^{N_d} |Cf_0(r_d^j, \theta_d^j, z_d^j, \alpha_d^j)|^2 + \frac{\gamma_f}{N_f} \sum_{j=1}^{N_f} \left\{ |Cf_1(r_f^j, \theta_f^j, z_f^j, \alpha_f^j)|^2 + |Cf_2(r_f^j, \theta_f^j, z_f^j, \alpha_f^j)|^2 + |Cf_3(r_f^j, \theta_f^j, z_f^j, \alpha_f^j)|^2 \right\} + \frac{\gamma_b}{N_{bs}} \sum_{j=1}^{N_{bs}} \left\{ |Cf_4(r_{bs}^j, \theta_{bs}^j, z_{bs}^j, \alpha_{bs}^j)|^2 + |Cf_5(r_{bs}^j, \theta_{bs}^j, z_{bs}^j, \alpha_{bs}^j)|^2 \right\} + \frac{\gamma_{bt}}{N_{bt}} \sum_{j=1}^{N_{bt}} |Cf_6(r_{bt}^j, \theta_{bt}^j, z_{bt}^j, \alpha_{bt}^j)|^2 \quad (12)$$

$$Cf_0 = (u', v') - (u, v) \Big|_{r_d, \theta_d, z_d, \alpha_d} \quad (13)$$

where the additional cost function Cf_0 includes training data with sampled points N_d ; N_f refers to the sampled points from physics-based equations and the semi-empirical (or purely empirical) formulas; N_{bs} and N_{bt} represent sampled points from surface and top boundary conditions, respectively; and $\gamma_d, \gamma_f, \gamma_b$ are contribution weights of the training data from field measurements or numerical simulations, physics-based equations, and boundary conditions, respectively. In this study, the Xavier’s normal initialization algorithm is adopted to initialize the network [62]. The numbers of randomly distributed spatial points within a region of $0 \leq \theta \leq 360^\circ, 0 < r \leq 1000km$, and $0 \leq z \leq 1500m$ are $N_d = 10,000, N_f = 100,000, N_{bs} = 5000$, and $N_{bt} = 5000$. The limited-memory Broyden–Fletcher–Goldfarb–Shanno (L-BFGS) optimization algorithm was selected to minimize the total loss function [63,64]. The automatic differentiation, which is readily available in several machine learning packages such as Tensorflow [65], was employed to compute the necessary derivatives of the output with respect to the input in the physics-based equations and/or semi-empirical formulas.

3.2. Risk Assessment

The developed KEDL can be effectively utilized for ETC wind risk assessment due to its efficiency.

3.2.1. Synthetic ETC Track

A statistical-based approach for the ETC wind risk assessment is adopted in a similar fashion for the simulation of hurricane wind risk [57,66,67]. The generation of the synthetic ETC tracks (also denoted as SynthETC) consists of four main components, namely genesis, tracking, intensity (in terms of central pressure), and termination [2]. Accordingly, the information projection from a wider geographic domain onto the target region can be achieved. Two independent climate covariates are used in SynthETC, namely El Nino/Southern Oscillation (ENSO) via the Nino3.4 index and the monthly North Atlantic Oscillation (NAO) index. While the local regression has been used for the modeling of genesis, tracking, and termination, the intensity was modeled via a weighted sampling scheme [2]. It should be noted that the SynthETC database has been trained on ETC tracks extracted from ERA-Interim meteorological reanalysis data from 1979 to 2015. The synthetic tracks include 6-hourly ETC center latitude and longitude, time, and central pressure deficit. The full-track synthetic ETC is then coupled with the developed KEDL-based wind model to generate large sets of synthetic ETC wind and pressure fields, as illustrated in Figure 4.

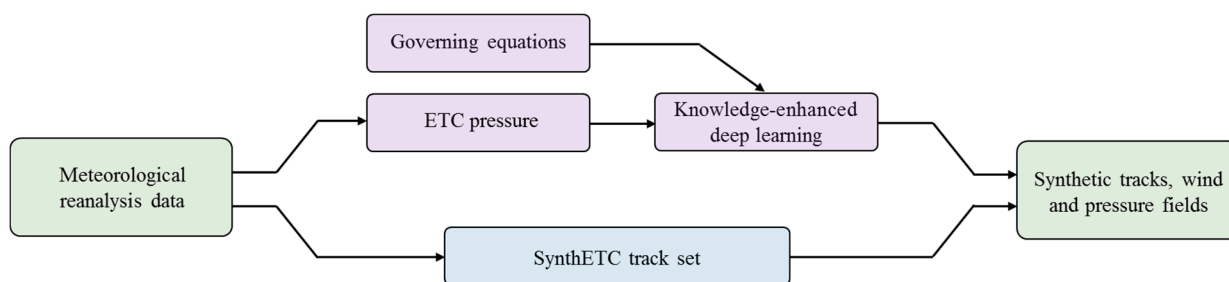


Figure 4. Schematic of knowledge-enhanced deep learning for the simulation of ETC wind risk.

3.2.2. ETC Wind Hazard

The estimated ETC wind hazard can be obtained through the mean recurrence interval (MRI), an important parameter in the risk assessment methodology. More specifically, hazard levels are assessed based on the annual exceedance probability and then arranged in terms of MRI or the return period. The MRI of a given wind speed V at a selected site is determined based on the following formula [68]:

$$MRI(v_i > V) = \frac{1}{\lambda P(v_i > V)} \tag{14}$$

where $P(v_i > V)$ = probability that the peak wind speed v_i is larger than a given threshold wind speed V ; and λ = mean annual occurrence rate of ETC wind speeds at the selected site.

4. Results and Discussion

4.1. Model Validation

The trained KEDL for simulation of ETC boundary-layer winds is validated based on reanalysis data of two ETCs which occurred on 19 February 2004 (ETC #1) and 17 December 2006 (ETC #2), respectively. The reanalysis data were retrieved from the ETC Atlas [28]. The comparison between the observed and simulated wind speeds at the lowest near-surface winds (925 hPa level) is depicted in Figure 5. The observed maximum wind speeds at the radius of maximum winds are 46 m/s and 34 m/s for ETC #1 and ETC #2, respectively, while the corresponding simulated wind speeds are 47 m/s and 35 m/s. The simulated and observed wind fields present similar shapes in terms of magnitude and location of the maximum wind speed, indicating that the proposed KEDL model captures the key

wind features inside the ETC boundary layer. Some discrepancies between simulations and observations can be noted, mainly due to the idealized pressure profile and simplified governing equations. In addition, the ETC thermodynamics could potentially modify the boundary-layer wind field. While only the dynamics-based equations are integrated into the KEDL architecture in the current study, a key advantage of the proposed KEDL is that it can always be retrained further (using weights and biases of current KEDL as initial ones of updated KEDL) once improved knowledge (e.g., more accurate pressure distribution and ETC dynamics) and/or additional knowledge (e.g., ETC thermodynamics and wind shear) is available.

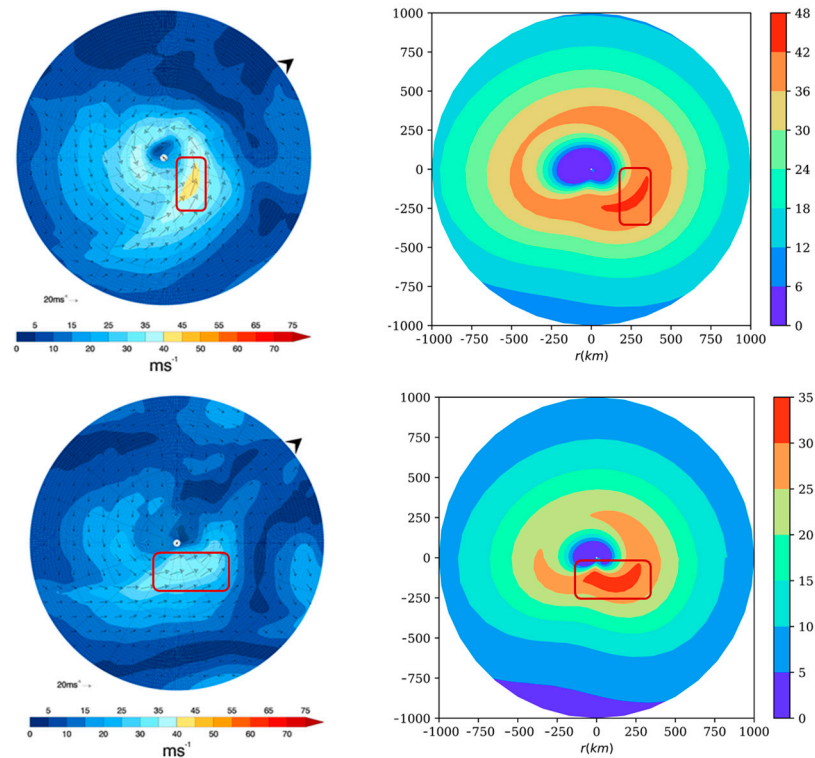


Figure 5. Comparison between reanalysis (left) (Dacre et al. 2012) and simulated (right) wind fields of ETC #1 (2004) (top) and ETC #2 (2006) (bottom) (Note: the red rectangles indicate the region of the most destructive winds).

4.2. Model Application

In this study, three ETC scenarios corresponding to storm parameters listed in Table 1 are investigated.

Table 1. ETC parameters for wind field simulation.

Parameter	Δp (hpa)	c (m/s)	θ_0 ($^\circ$)	ϕ ($^\circ$)	z_0 (m)
scenario 1	80	10	50	45	0.001
scenario 2	60	8	70	45	0.01
scenario 3	40	6	90	45	0.1

Figure 6 depicts the 3D shaded surfaces of simulated wind speed along with the contours of simulated vertical wind profile at the East location (relative to the approach angle). The simulation results indicate that the height of maximum wind decreases with the wind speed. Furthermore, an increase of surface roughness leads to a rapid decrease of wind speed from the ground surface, and an increase of central pressure difference results in an increase of wind speed. The supergradient winds, commonly observed in the TC boundary layer, are weak in the case of ETC, as shown by Figure 6.

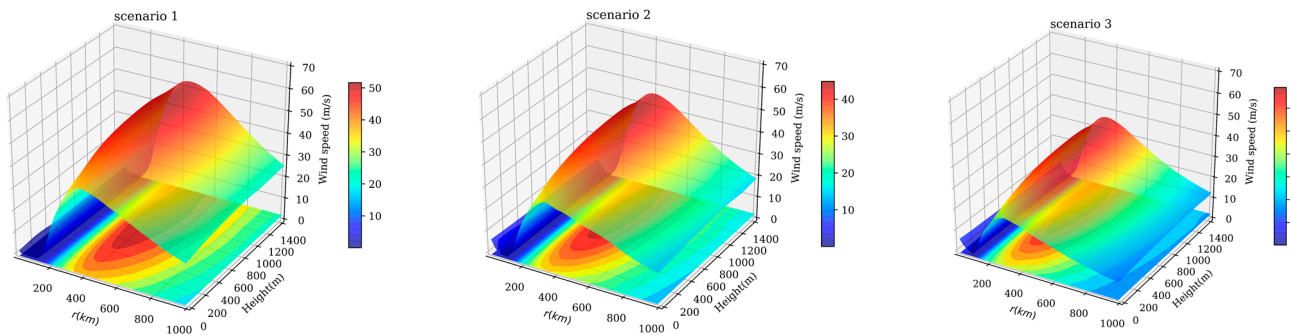


Figure 6. Three-dimensional shaded surfaces of simulated wind speed along with vertical wind profile contours.

On the other hand, Figure 7 presents the spatial distribution of simulated wind speed at three different levels (i.e., 10 m, 500 m, and 1000 m) with $\Delta p = 50hpa$, $\varphi = 40^\circ$, $c = 10m/s$, $\theta_0 = 35^\circ$, and $z_0 = 0.01m$. The simulation results indicate that the spatial distribution of the wind field inside ETC presents a comma-like shape, which is a common feature of ETC boundary-layer winds.

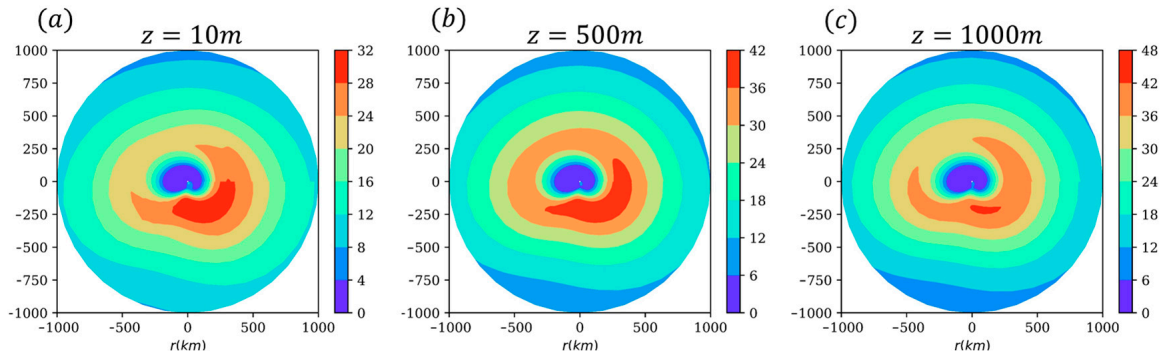


Figure 7. Spatial distribution of the ETC wind at three different altitudes: (a) $z = 10\text{ m}$; (b) $z = 500\text{ m}$; and (c) $z = 1000\text{ m}$.

4.3. Risk Analysis

The MRI distribution of the 10 m-height ETC wind speeds at two selected points $(31.23^\circ; 81.28^\circ)$ and $(43.00^\circ; 70.74^\circ)$, located in the US southeast and northeast, were accordingly constructed and depicted in a logarithmic scale as shown in Figure 8. According to Figure 8, the MRI distribution of wind speed at location $(43.00^\circ; 70.74^\circ)$ is higher than that at location $(31.23^\circ; 81.28^\circ)$. This observation is expected, since the northeast location is more frequently impacted by nor'easters compared to the southeast location.

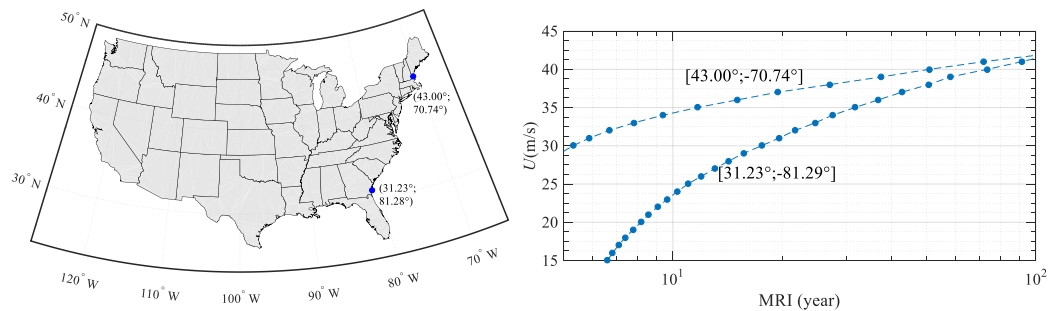


Figure 8. Location of the two selected points (left) along with MRI distribution of wind speed (at 10 m height) (right).

5. Concluding Remarks

In this study, a knowledge-enhanced deep learning (KEDL) has been proposed to provide the three-dimensional (3D) boundary-layer wind field with high computational efficiency and accuracy for an arbitrary ETC using several storm parameters (i.e., central pressure difference, translational speed, approach angle, latitude of ETC center, and surface roughness) as network inputs. The KEDL wind model effectively leverages the rationalism-based knowledge in terms of the scale-analysis-based reduced-order Navier–Stokes equations that governs the ETC wind field and the empiricism-based knowledge in terms of ERA-Interim reanalysis data-based two-dimensional (2D) parametric formula (with respect to radial and azimuthal coordinates) that prescribes an asymmetric ETC pressure field, and hence enhances the purely data-driven methodology. The developed KEDL-based ETC wind model shows good simulation results by presenting similar shapes in terms of magnitude and location of the maximum wind speed, indicating the proposed KEDL model captures the essential wind features inside the ETC boundary layer. However, some discrepancies between simulations and observations can still be noted, due mainly to the idealized pressure profile and simplified governing equations. In addition, the ETC thermodynamics could potentially modify the boundary-layer wind field. While only the dynamics-based equations are integrated into the KEDL architecture in the current study, a key advantage of the proposed KEDL is that it can always be retrained further (using weights and biases of current KEDL as initial ones of updated KEDL) once improved knowledge (e.g., more accurate pressure distribution and ETC dynamics) and/or additional knowledge (e.g., ETC thermodynamics and wind shear) is available. Due to its high efficiency and accuracy, the KEDL wind model can be readily utilized in conjunction with a large set of stochastic tracks under the ETC risk analysis framework. Hence, this study offers an effective approach to assess ETC wind risk along the US northeast coast.

Author Contributions: Conceptualization, R.S. and T.W.; methodology, R.S. and T.W.; software, R.S.; validation, R.S. and T.W.; formal analysis, R.S. and T.W.; investigation, R.S. and T.W.; resources, R.S. and T.W.; data curation, R.S.; writing—original draft preparation, R.S. and T.W.; writing—review and editing, R.S. and T.W.; visualization, R.S. and T.W.; supervision, T.W.; project administration, R.S. and T.W.; funding acquisition, T.W. All authors have read and agreed to the published version of the manuscript.

Funding: This research was funded by the National Science Foundation grant # CMMI 2011396.

Institutional Review Board Statement: Not applicable.

Informed Consent Statement: Not applicable.

Data Availability Statement: Not applicable.

Acknowledgments: The authors are deeply grateful to Timothy Hall and James F. Booth for providing the synthetic track database for the ETC risk simulation.

Conflicts of Interest: The authors declare no conflict of interest.

References

1. Von Ahn, J.U.; Sienkiewicz, J.M.; Copridge, J.; Min, J.; Crutch, T. Hurricane force extratropical cyclones as observed by the QuikSCAT scatterometer. In Preprint 8th Symposium on Integrated Observing and Assimilation Systems for Atmosphere, Oceans and Land Surface. *AMS Annu. Meet.* **2004**, *12*, 2004.
2. Hall, T.; Booth, J.F. SynthETC: A statistical model for severe winter storm hazard on eastern North America. *J. Clim.* **2017**, *30*, 5329–5343. [[CrossRef](#)]
3. Shimkus, C.E.; Ting, M.; Booth, J.F.; Adamo, S.B.; Madajewicz, M.; Kushnir, Y.; Rieder, H.E. Winter storm intensity, hazards, and property losses in the New York tristate area. *Ann. N. Y. Acad. Sci.* **2017**, *1400*, 65–80. [[CrossRef](#)]
4. Kunkel, K.E.; Easterling, D.R.; Kristovich, D.A.; Gleason, B.; Stoecker, L.; Smith, R. Meteorological causes of the secular variations in observed extreme precipitation events for the conterminous United States. *J. Hydrometeorol.* **2012**, *13*, 1131–1141. [[CrossRef](#)]
5. Booth, J.F.; Rieder, H.E.; Kushnir, Y. Comparing hurricane and extratropical storm surge for the Mid-Atlantic and Northeast Coast of the United States for 1979–2013. *Environ. Res. Lett.* **2016**, *11*, 094004. [[CrossRef](#)]

6. Wu, T.; Kareem, A.; Li, S. On the excitation mechanisms of rain–wind induced vibration of cables: Unsteady and hysteretic nonlinear features. *J. Wind Eng. Ind. Aerodyn.* **2013**, *122*, 83–95. [[CrossRef](#)]
7. Snaiki, R.; Wu, T.; Whittaker, A.S.; Atkinson, J.F. Hurricane wind and storm surge effects on coastal bridges under a changing climate. *Trans. Res. Rec.* **2020**, *2674*, 23–32. [[CrossRef](#)]
8. Vickery, P.J.; Wadhera, D.; Powell, M.D.; Chen, Y. A hurricane boundary layer and wind field model for use in engineering applications. *J. Appl. Meteorol. Climatol.* **2009**, *48*, 381–405. [[CrossRef](#)]
9. Snaiki, R.; Wu, T. A semi-empirical model for mean wind velocity profile of landfalling hurricane boundary layers. *J. Wind Eng. Ind. Aerodyn.* **2018**, *180*, 249–261. [[CrossRef](#)]
10. Shapiro, L.J. The asymmetric boundary layer flow under a translating hurricane. *J. Atmos. Sci.* **1983**, *40*, 1984–1998. [[CrossRef](#)]
11. Vickery, P.J.; Twisdale, L.A. Wind-field and filling models for hurricane wind-speed predictions. *J. Struct. Eng.* **1995**, *121*, 1700–1709. [[CrossRef](#)]
12. Kepert, J. The dynamics of boundary layer jets within the tropical cyclone core. Part I: Linear theory. *J. Atmos. Sci.* **2001**, *58*, 2469–2484. [[CrossRef](#)]
13. Snaiki, R.; Wu, T. A linear height-resolving wind field model for tropical cyclone boundary layer. *J. Wind Eng. Ind. Aerodyn.* **2017**, *171*, 248–260. [[CrossRef](#)]
14. Snaiki, R.; Wu, T. Modeling tropical cyclone boundary layer: Height-resolving pressure and wind fields. *J. Wind Eng. Ind. Aerodyn.* **2017**, *170*, 18–27. [[CrossRef](#)]
15. Adamson, D.S.; Belcher, S.E.; Hoskins, B.J.; Plant, R.S. Boundary-layer friction in midlatitude cyclones. *Q. J. R. Meteorol. Soc. A J. Atmos. Sci. Appl. Meteorol. Phys. Oceanogr.* **2006**, *132*, 101–124. [[CrossRef](#)]
16. Beare, R.J. Boundary layer mechanisms in extratropical cyclones. *Q. J. R. Meteorol. Soc. A J. Atmos. Sci. Appl. Meteorol. Phys. Oceanogr.* **2007**, *133*, 503–515. [[CrossRef](#)]
17. Huang, W.F.; Xu, Y.L. Prediction of typhoon design wind speed and profile over complex terrain. *Struct. Eng. Mech.* **2013**, *45*, 1–18. [[CrossRef](#)]
18. Wei, C.C.; Peng, P.C.; Tsai, C.H.; Huang, C.L. Regional Forecasting of Wind Speeds during Typhoon Landfall in Taiwan: A Case Study of Westward-Moving Typhoons. *Atmosphere* **2018**, *9*, 141. [[CrossRef](#)]
19. Shamshirband, S.; Rabczuk, T.; Chau, K.W. A survey of deep learning techniques: Application in wind and solar energy resources. *IEEE Access* **2019**, *7*, 164650–164666. [[CrossRef](#)]
20. Banan, A.; Nasiri, A.; Taheri-Garavand, A. Deep learning-based appearance features extraction for automated carp species identification. *Aquac. Eng.* **2020**, *89*, 102053. [[CrossRef](#)]
21. Fan, Y.; Xu, K.; Wu, H.; Zheng, Y.; Tao, B. Spatiotemporal modeling for nonlinear distributed thermal processes based on KL decomposition, MLP and LSTM network. *IEEE Access* **2020**, *8*, 25111–25121. [[CrossRef](#)]
22. Wu, T.; Snaiki, R. Applications of Machine Learning to Wind Engineering. *Front. Built Environ.* **2022**, *8*, 811460. [[CrossRef](#)]
23. Swischuk, R.; Mainini, L.; Peherstorfer, B.; Willcox, K. Projection-Based Model Reduction: Formulations for Physics-Based Machine Learning. *Comput. Fluids* **2019**, *179*, 704–717. [[CrossRef](#)]
24. Dissanayake, M.W.M.G.; Phan-Thien, N. Neural-network-based approximations for solving partial differential equations. *Commun. Numer. Methods Eng.* **1994**, *10*, 195–201. [[CrossRef](#)]
25. Raissi, M.; Perdikaris, P.; Karniadakis, G.E. Physics Informed Deep Learning (Part I): Data-driven solutions of nonlinear partial differential equations. *arXiv* **2017**, arXiv:1711.10561.
26. Raissi, M.; Perdikaris, P.; Karniadakis, G.E. Physics informed deep learning (Part II): Data-driven discovery of nonlinear partial differential equations. *arXiv* **2017**, arXiv:1711.10566.
27. Snaiki, R.; Wu, T. Knowledge-enhanced deep learning for simulation of tropical cyclone boundary-layer winds. *J. Wind Eng. Ind. Aerodyn.* **2019**, *194*, 103983. [[CrossRef](#)]
28. Dacre, H.F.; Hawcroft, M.K.; Stringer, M.A.; Hodges, K.I. An extratropical cyclone atlas: A tool for illustrating cyclone structure and evolution characteristics. *Bull. Am. Meteorol. Soc.* **2012**, *93*, 1497–1502. [[CrossRef](#)]
29. Dolan, R.; Davis, R.E. An intensity scale for Atlantic coast northeast storms. *J. Coast. Res.* **1992**, *8*, 840–853.
30. Butman, B.; Sherwood, C.R.; Dalyander, P.S. Northeast storms ranked by wind stress and wave-generated bottom stress observed in Massachusetts Bay, 1990–2006. *Cont. Shelf Res.* **2008**, *28*, 1231–1245. [[CrossRef](#)]
31. Birchler, J.J.; Dalyander, P.S.; Stockdon, H.F.; Doran, K.S. *National Assessment of Nor'easter-Induced Coastal Erosion Hazards: Mid-and Northeast Atlantic Coast*; US Geological Survey: Reston, VA, USA, 2015; Open-File Report No. 2015-1154.
32. Zhang, K.; Douglas, B.C.; Leatherman, S.P. Beach erosion potential for severe nor'easters. *J. Coast. Res.* **2001**, *17*, 309–321.
33. Ulbrich, U.; Leckebusch, G.C.; Pinto, J.G. Extra-tropical cyclones in the present and future climate: A review. *Theor. Appl. Climatol.* **2009**, *96*, 117–131. [[CrossRef](#)]
34. Bjerknes, J.; Solberg, H. Life cycle of cyclones and the polar front theory of atmospheric circulation. *Geophys. Publ.* **1922**, *3*, 3–17.
35. Shapiro, M.A.; Keyser, D. Fronts, jet streams and the tropopause. In *Extratropical Cyclones*; American Meteorological Society: Boston, MA, USA, 1990; pp. 167–191.
36. Bauer, M.; Del Genio, A.D. Composite analysis of winter cyclones in a GCM: Influence on climatological humidity. *J. Clim.* **2006**, *19*, 1652–1672. [[CrossRef](#)]
37. Chang, E.K.; Song, S. The seasonal cycles in the distribution of precipitation around cyclones in the western North Pacific and Atlantic. *J. Atmos. Sci.* **2006**, *63*, 815–839. [[CrossRef](#)]

38. Rudeva, I.; Gulev, S.K. Composite analysis of North Atlantic extratropical cyclones in NCEP–NCAR reanalysis data. *Mon. Weather Rev.* **2011**, *139*, 1419–1446. [[CrossRef](#)]
39. Sinclair, M.R.; Revell, M.J. Classification and composite diagnosis of extratropical cyclogenesis events in the southwest Pacific. *Mon. Weather Rev.* **2000**, *128*, 1089–1105. [[CrossRef](#)]
40. McLay, J.G.; Martin, J.E. Surface cyclolysis in the North Pacific Ocean. Part III: Composite local energetics of tropospheric-deep cyclone decay associated with rapid surface cyclolysis. *Mon. Weather Rev.* **2002**, *130*, 2507–2529. [[CrossRef](#)]
41. Hoskins, B.J.; Hodges, K.I. New perspectives on the Northern Hemisphere winter storm tracks. *J. Atmos. Sci.* **2002**, *59*, 1041–1061. [[CrossRef](#)]
42. Hoskins, B.J.; Hodges, K.I. A new perspective on Southern Hemisphere storm tracks. *J. Clim.* **2005**, *18*, 4108–4129. [[CrossRef](#)]
43. Simmons, A. ERA-Interim: New ECMWF reanalysis products from 1989 onwards. *ECMWF Newsl.* **2006**, *110*, 25–36.
44. Dee, D.P.; Uppala, S.M.; Simmons, A.J.; Berrisford, P.; Poli, P.; Kobayashi, S.; Andrae, U.; Balmaseda, M.A.; Balsamo, G.; Bauer, D.P.; et al. The ERA-Interim Reanalysis: Configuration and Performance of the Data Assimilation System. *Q. J. R. Meteorol. Soc.* **2011**, *137*, 553–597. [[CrossRef](#)]
45. Wang, C.C.; Rogers, J.C. A composite study of explosive cyclogenesis in different sectors of the North Atlantic. Part I: Cyclone structure and evolution. *Mon. Weather Rev.* **2001**, *129*, 1481–1499. [[CrossRef](#)]
46. Catto, J.L.; Shaffrey, L.C.; Hodges, K.I. Can climate models capture the structure of extratropical cyclones? *J. Clim.* **2010**, *23*, 1621–1635. [[CrossRef](#)]
47. Russell, L.R. Probability distributions for hurricane effects. *J. Waterways Harbors. Coast. Eng. Div.* **1971**, *97*, 139–154. [[CrossRef](#)]
48. FEMA. *Region II Storm Surge Project—Joint Probability Analysis of Hurricane and Extratropical Flood Hazards September 2014*; Report prepared for Federal Emergency Management Agency; HSFE02-09-J-001; FEMA: Washington, DC, USA, 2014.
49. Catalano, A.J.; Broccoli, A.J.; Kapnick, S.B.; Janoski, T.P. High-impact extratropical cyclones along the northeast coast of the United States in a long-coupled climate model simulation. *J. Clim.* **2019**, *32*, 2131–2143. [[CrossRef](#)]
50. Kumler-Bonfanti, C.; Stewart, J.; Hall, D.; Govett, M. Tropical and extratropical cyclone detection using deep learning. *J. Appl. Meteorol. Climatol.* **2020**, *59*, 1971–1985. [[CrossRef](#)]
51. Lu, C.; Kong, Y.; Guan, Z. A mask R-CNN model for reidentifying extratropical cyclones based on quasi-supervised thought. *Sci. Rep.* **2020**, *10*, 15011. [[CrossRef](#)]
52. Shi, M.; He, P.; Shi, Y. Detecting extratropical cyclones of the northern hemisphere with single shot detector. *Remote Sens.* **2022**, *14*, 254. [[CrossRef](#)]
53. Xu, G.; Han, G.; Dong, C.; Yang, J.; DeYoung, B. Observing and Modeling the Response of Placentia Bay to an Extratropical Cyclone. *Atmosphere* **2019**, *10*, 724. [[CrossRef](#)]
54. Economou, T.; Stephenson, D.B.; Ferro, C.A. Spatio-temporal modelling of extreme storms. *Ann. Appl. Stat.* **2014**, *8*, 2223–2246. [[CrossRef](#)]
55. Meng, Y.; Matsui, M.; Hibi, K. An analytical model for simulation of the wind field in a typhoon boundary layer. *J. Wind Eng. Ind. Aerodyn.* **1995**, *56*, 291–310. [[CrossRef](#)]
56. Holland, G.J. An analytic model of the wind and pressure profiles in hurricanes. *Mon. Weather Rev.* **1980**, *108*, 1212–1218. [[CrossRef](#)]
57. Snaiki, R.; Wu, T. Revisiting hurricane track model for wind risk assessment. *Struct. Saf.* **2020**, *87*, 102003. [[CrossRef](#)]
58. Levenberg, K. A method for the solution of certain non-linear problems in least squares. *Q. Appl. Math.* **1944**, *2*, 164–168. [[CrossRef](#)]
59. Marquardt, D.W. An algorithm for least-squares estimation of nonlinear parameters. *J. Soc. Ind. Appl. Math.* **1963**, *11*, 431–441. [[CrossRef](#)]
60. Wu, T.; Kareem, A. Modeling hysteretic nonlinear behavior of bridge aerodynamics via cellular automata nested neural network. *J. Wind Eng. Ind. Aerodyn.* **2011**, *99*, 378–388. [[CrossRef](#)]
61. Bardenet, R.; Brendel, M.; Kégl, B.; Sebag, M. February. Collaborative hyperparameter tuning. In Proceedings of the International Conference on Machine Learning, PMLR, Atlanta, GA, USA, 16–21 June 2013; pp. 199–207.
62. Glorot, X.; Bengio, Y. Understanding the difficulty of training deep feedforward neural networks. In Proceedings of the Thirteenth International Conference on Artificial Intelligence and Statistics, PMLR, Chia Laguna Resort, Sardinia, Italy, 13–15 March 2010; pp. 249–256.
63. Liu, D.C.; Nocedal, J. On the limited memory BFGS method for large scale optimization. *Math. Program.* **1989**, *45*, 503–528. [[CrossRef](#)]
64. Byrd, R.H.; Lu, P.; Nocedal, J.; Zhu, C. A limited memory algorithm for bound constrained optimization. *SIAM J. Sci. Comput.* **1995**, *16*, 1190–1208. [[CrossRef](#)]
65. Abadi, M.; Barham, P.; Chen, J.; Chen, Z.; Davis, A.; Dean, J.; Devin, M.; Ghemawat, S.; Irving, G.; Isard, M.; et al. Tensorflow: A system for large-scale machine learning. In Proceedings of the 12th USENIX Symposium on Operating Systems Design and Implementation (OSDI 16), Savannah, GA, USA, 2–4 November 2016; pp. 265–283.
66. Vickery, P.J.; Skerlj, P.F.; Twisdale, L.A. Simulation of hurricane risk in the US using empirical track model. *J. Struct. Eng.* **2000**, *126*, 1222–1237. [[CrossRef](#)]

-
67. Hall, T.M.; Jewson, S. Statistical modelling of North Atlantic tropical cyclone tracks. *Tellus A Dyn. Meteorol. Oceanogr.* **2007**, *59*, 486–498. [[CrossRef](#)]
 68. Pei, B.; Pang, W.; Testik, F.Y.; Ravichandran, N.; Liu, F. Mapping joint hurricane wind and surge hazards for Charleston, South Carolina. *Nat. Hazards* **2014**, *74*, 375–403. [[CrossRef](#)]